









Cite this: *Phys. Chem. Chem. Phys.*,
2025, 27, 17008

Surface migration of chloride ions on natural salts by ammonia and water vapor under low RH conditions†

Nicolas Fauré, ^a Markus Hartmann, ^{‡a} Ivan Gladich, ^{bc} Andrey Shavorskiy, ^d
Erik S. Thomson ^{*a} and Xiangrui Kong ^{*a}

Natural salts are minerals formed through natural processes, generally consisting of complex mixtures of ions. In the atmosphere, natural salts are present as aerosol particles, originating from both marine and terrestrial sources. The interaction of these natural salt particles with trace gases, also termed ageing, can influence various atmospheric processes such as cloud properties or atmospheric chemistry. However, our understanding of these interactions, particularly at low relative humidity (RH) well below deliquescence conditions, when particles are in the solid state, remains limited. This study investigates phenomena occurring on surfaces of two polycrystalline solid natural salt samples upon exposure to ammonia (NH₃) and low RH conditions. Surface structures and chemical compositions, at nanometre-scale depths, were measured using X-ray photoelectron spectroscopy (XPS) and near edge X-ray absorption fine structure (NEXAFS) spectroscopy at a synchrotron-based ambient pressure XPS (APXPS) endstation. The findings indicate that the addition of NH₃ to a humidified atmosphere leads to an enrichment of chloride (Cl[−]) on the surface of the solid natural salt samples. We propose that the formation of ammonium (NH₄⁺) from NH₃ uptake on the sample surfaces causes the migration of Cl[−] to the surface, which appears to outcompete other anions such as sulfate (SO₄^{2−}) for cation–anion neutralization. This surface enrichment of Cl[−] indicates potential dechlorination processes, highlighting how anthropogenic emissions, here NH₃, can affect the properties of solid natural salt particles.

Received 16th March 2025,
Accepted 16th July 2025

DOI: 10.1039/d5cp01025j

rsc.li/pccp

1. Introduction

Natural salts are minerals often consisting of complex mixtures of ions that are generally found in the lithosphere and the atmosphere. In the lithosphere, these salts are present as deposits from water evaporation, such as salt pans or dry lakes (playas). In the atmosphere, these salts appear as aerosol particles, arising from marine sources like sea salt and from terrestrial sources through phenomena such as wind lofting of salt deposits or blowing snow events.^{1,2} Because these aerosol

particles are directly emitted into the atmosphere, they are termed primary natural salt particles. Marine sources are globally the most abundant source of primary natural salt particles, but terrestrial sources can be significant regionally, such as in arid regions and populated areas with little influence from marine air masses.^{2,3} In arid regions, primary natural salt particles often appear as salts mixed with mineral dust particles.^{4,5} The ionic composition of these particles, from marine and terrestrial sources, is often dominated by sodium (Na⁺), chloride (Cl[−]), sulfate (SO₄^{2−}) and magnesium (Mg²⁺) ions.^{6–8} However, the properties of these particles change over time as they undergo physicochemical modifications when interacting with atmospheric gas-phase compounds, including water vapor and ammonia among many others. These modifications, known as ageing, influence many atmospheric processes such as cloud properties and atmospheric chemistry.

Water vapor is ubiquitous in the atmosphere with relative humidity (RH) levels ranging from nearly 0% to more than 100%. Due to this large range, water vapor uptake on primary natural salt particles can impact both their surface and bulk physicochemical properties. The hygroscopic nature of these particles allows significant water uptake on their surfaces to

^a Department of Chemistry and Molecular Biology, Atmospheric Science, University of Gothenburg, 41390 Gothenburg, Sweden. E-mail: erik.thomson@chem.gu.se, kongx@chem.gu.se

^b Qatar Environment and Energy Research Institute, Hamad Bin Khalifa University, 31110 Doha, Qatar

^c Department of Pure and Applied Sciences, University of Urbino Carlo Bo, 61028, Italy

^d MAX IV Laboratory, Lund University, 22100 Lund, Sweden

† Electronic supplementary information (ESI) available. See DOI: <https://doi.org/10.1039/d5cp01025j>

‡ Present address: Department for Atmospheric Microphysics, Leibniz Institute for Tropospheric Research, 04318 Leipzig, Germany.



occur, even at low RH levels, when the particles remain in a solid state. Water uptake on solid primary natural salt particles leads to changes in their surface properties such as structure, chemical composition and chemical reactivity. Structural modifications can manifest as various phenomena including hydrate formation or predeliquescence.^{9,10} Chemical composition can be altered through various processes, such as preferential cation-anion interactions, ion transport through grain boundaries to the surface or ion competition for solvation.^{11–13} Chemical reactivity can increase upon water vapor uptake, leading to spontaneous and heterogeneous surface chemistry.^{14–16} This enhanced reactivity can further promote the uptake of trace gases.^{17,18} Notably, the presence of electric fields on the surface appears to contribute to this increased reactivity.^{19,20}

Ammonia (NH_3) is a major air pollutant primarily emitted by anthropogenic activities such as animal husbandry and by fertilizers in agriculture, with annual emissions estimated to exceed 58 million tons.²¹ As the principal base in the atmosphere, NH_3 is a major component of acid-base neutralization reactions with gas-phase acids present in the atmosphere. These neutralization reactions contribute to the formation of secondary inorganic aerosols (SIAs), such as ammonium sulfate ($(\text{NH}_4)_2\text{SO}_4$), ammonium bisulfate ($(\text{NH}_4)\text{HSO}_4$), ammonium nitrate (NH_4NO_3) and ammonium chloride (NH_4Cl), affecting the gas-to-particle partitioning of their gas-phase precursors.^{22,23} Additionally, NH_3 is a highly soluble base (Henry's law constant ranging from 30 to 90 mol L^{-1} atm $^{-1}$ at 298 K), which promotes its uptake in aqueous droplets, especially under acidic conditions that facilitate ammonium (NH_4^+) formation.²⁴ In aqueous solution, NH_4^+ can affect surface composition through preferential charge neutralization. For example, migration of bromide (Br^-) ions to the surface of aqueous solutions was observed in the presence of a tetrabutylammonium surfactant.²⁵ In aqueous aerosol particles, phenomena that induce surface enhancement of halogen species can lead to an increased formation of halogenated gases.^{26–29} This has critical implications for atmospheric chemistry, particularly in relation to stratospheric ozone depletion.³⁰ However, these phenomena should not be limited to aqueous systems, as water vapor uptake on aerosol particles, notably on solid primary natural salt particles, occurs at low RH well below deliquescence.^{11,12}

In this study, we investigate surface phenomena occurring on two polycrystalline solid natural salt samples upon exposure to ammonia at low RH levels. The natural salt samples were collected from a dry lake bed (Dalangtan Playa) and a saline lake (Mang'ai Salt Lake) in the Qaidam Basin, China. The structural and chemical composition of the natural salt surfaces, at a nanometer-scale depth, were measured by X-ray photoelectron spectroscopy (XPS) and partial Auger–Meitner electron yield near edge X-ray absorption fine structure (NEXAFS) spectroscopy at a synchrotron-based ambient pressure XPS (APXPS) endstation. This investigation provides insights into surface ageing processes of solid primary natural salt particles upon exposure to gas-phase compounds from anthropogenic emissions. As aerosol particles originating from North and Western China represent an important source of particulate matter across major cities in East Asia

and even North America, the samples and conditions used here provide a crucial case for understanding the impact of primary natural salt particle ageing on atmospheric processes both regionally and globally.^{31–33}

2. Sampling and methodology

2.1 Sample collection

The natural salt samples used in this study were collected from the Qaidam Basin, located on the Northeastern Qinghai-Xizang Plateau. The Qaidam Basin is an arid region where primary natural salt particles are mainly generated through wind lofting. From May 1st to 9th 2022, an extensive field campaign was conducted in this region to collect various samples, including brines, lakebed salts, crust salts, playa salts, and distinct layered hydrated salts. In this study, we focused on a playa salt and a brine sample, which were collected from the Dalangtan (DLT) Playa ($38^\circ 4' 33''\text{N}$, $90^\circ 59' 46''\text{E}$) and the Mang'ai (MA) Salt Lake ($38^\circ 32' 16''\text{N}$, $91^\circ 23' 34''\text{E}$), respectively. The brine sample from the MA Salt Lake was collected from 2–5 cm below the surface, and the playa salt from DLT Playa was collected from the DLT Playa ground.³⁴ All samples were stored in polyethylene containers, covered with Parafilm and kept at 4 °C.

DLT Playa is a saline dry lake in the hyper-arid zone of the Qaidam Basin, spanning over approximately 500 km². This zone is marked by extremely low atmospheric pressure, high ultraviolet radiation, low annual mean temperatures and has large seasonal and diurnal temperature variations, and extremely low RH. Natural salt particles are formed under extreme aridity, making also DLT a potential analogue for Mars in the study of saline deposits and their evolution.³⁵ The geological history of DLT, shaped by tectonic activity and climatic shifts, further adds to its relevance as a site for understanding how natural salts accumulate and transform under hyper-arid conditions.³⁶

The MA Salt Lake is a saline lake, located near the Kunlun and Altyn Mountains, covers an area of about 26 km² and is underlain by a rock salt bed up to 9.7 m thick, signifying extensive salt accumulation under long-standing evaporative conditions. This thick salt bed and prolonged saline conditions make the MA Salt Lake an excellent site for studying saline lake dynamics and how these lakes contribute to the production of primary natural salt particles.

2.2 Chemical composition

The brine from the MA Salt Lake and the dissolved salt from DLT Playa went through a filtration process prior to analysis. Filtration involved the passage of samples through a filter paper with pore sizes of <20 μm followed by a finer filtration using 0.22 μm water filtration membranes. To meet the detection limits of ion chromatography (IC), the solution with dissolved DLT Playa salt was diluted 2000-fold, and the brine from the MA Salt Lake was diluted 1500-fold. Bulk analysis was conducted using a thermo Fisher scientific IC system (DX 600), which measured various cations (K^+ , Na^+ , Mg^{2+} , Ca^{2+} , and



Table 1 Ionic molar fractions of MA Salt Lake brine and DLT Playa salt

	Molar fraction	
	MA Salt Lake brine	DLT Playa salt
Na ⁺ (%)	17	50
K ⁺ (%)	2	0
Mg ²⁺ (%)	24	1
Cl ⁻ (%)	52	45
SO ₄ ²⁻ (%)	5	3

NH₄⁺) and anions (Cl⁻, SO₄²⁻, NO₃⁻, NO₂⁻, and F⁻) in the samples. Cations were analysed using a CS12A IC column (Dionex Ion Pac) with a 30 mM methanesulfonic acid (CH₃SO₃H) eluent, while anions were measured using an AS11-HC IC column (Dionex Ion Pac) with a 20 mM potassium hydroxide (KOH) eluent. The ionic molar fractions based on IC measurements are presented in Table 1.

2.3 XPS and NEXAFS measurements with APXPS

XPS and partial Auger–Meitner electron yield NEXAFS measurements were conducted with the synchrotron-based APXPS end-station at the HIPPIE beamline of MAX IV Laboratory. HIPPIE is a soft X-ray beamline located on the 3 GeV electron storage ring that can provide photon energies (PE) in the range 250–2200 eV at a flux superior to 10¹² photons s⁻¹. The APXPS instrument at the HIPPIE beamline features an analysis chamber with an integrated near ambient pressure cell, capable of accommodating condensed phase materials mounted on a sample holder and surrounded by a gaseous atmosphere at pressures up to 30 mbar. More details about the APXPS instrument at the HIPPIE beamline are provided by Zhu *et al.*³⁷ In our experiments, the dissolution of DLT Playa salt and dilution of MA Salt Lake brine were done using Milli-Q type 1 ultrapure water and the solutions were drop-cast onto different sample holders. The sample holders were subsequently heated to 40 °C to accelerate salt precipitation. This procedure yields a thin, uniform layer of salt crystals on the sample holder, minimizing issues such as differential charging and surface inhomogeneity during XPS measurements. Based on ionic molar fraction in Table 1, MA Salt Lake crystals are likely a mix of MgCl₂ with NaCl while DLT Playa crystals are mainly NaCl. After complete evaporation, sample holders were inserted into the near ambient pressure cell for experiments, one at a time, as this cell can only accommodate one sample holder. The analysis chamber was maintained under high vacuum conditions with a base pressure of 1 × 10⁻¹⁰ mbar before, after and during experiments. The gaseous atmosphere in our experiments was constituted either of pure water vapor (NH₃-free cases) or water vapor plus a mix of ammonia/nitrogen NH₃/N₂ (NH₃-exposed cases). The total maximum pressure in our experiments was 5 mbar. The mix of ammonia/nitrogen NH₃/N₂ was inserted into the near ambient pressure cell from a gas cylinder with a concentration of 1% NH₃ in N₂ by volume. Water vapor was introduced into the near ambient pressure cell from a degassed water source that had undergone three freeze–thaw–pump cycles. The RH inside the near ambient pressure cell was regulated by

adjusting the water vapor pressure using a leak valve, while sample temperature was held constant at 16 °C.

In XPS, the selected PE determines the kinetic energy (KE) of an emitted photoelectron as

$$KE = PE - BE - \sigma. \quad (1)$$

Here BE is the binding energy of electrons in atoms and σ the work function, which corresponds to the minimum energy needed to remove an electron outside a material's surface. The KE of a photoelectron is also related to its inelastic mean free path (IMFP), defined as the average distance an electron travel between two inelastic scattering processes (energy loss), as

$$IMFP = KE^y. \quad (2)$$

Here y is between 0.6 and 0.75 for most compounds.³⁸ This relationship shows that photoelectrons with higher KE exhibit longer IMFP, thereby traveling greater distances before undergoing an energy loss event. Additionally, the mean escape depth (MED) is defined as the average depth from which detected photoelectrons that have not undergone inelastic scattering originate, and is related to IMFP as

$$MED = IMFP \times \cos(\alpha). \quad (3)$$

Here α is the angle of photoelectron emission, which is 0° in this study, thus MED values are similar to IMFP. More details about IMFP and MED can be found in Powell *et al.*³⁹ Taking together, an increase in PE increases the KE of photoelectrons (eqn (1)), resulting in higher IMFP (eqn (2)) and higher MED (eqn (3)).

In our XPS measurement, we acquired both wide range spectra (also named survey spectra) and detailed, narrow band, single-edge spectra (high-energy resolution photoemission spectra). Survey spectra were acquired at PE = 1000 eV with the aim of giving an overview of surface elemental composition. High-energy resolution photoemission spectra were taken for different elements and orbitals including oxygen (O 1s), nitrogen (N 1s), carbon (C 1s), chlorine (Cl 2p), sulfur (S 2p), magnesium (Mg 2p) and sodium (Na 2s). For high-energy resolution photoemission spectra, the PE utilized for each element was adjusted to measure photoelectrons with four different kinetic energies, 300, 400, 500 and 600 eV, corresponding to MEDs of 1.1, 1.4, 1.5 and 1.7 nm, respectively. The MEDs were calculated with QUASES-IMFP-TPP2M version 3 software utilizing ammonium chloride (NH₄Cl) as the material of interest.⁴⁰ The signal intensity of the measured elements was normalized by photoionization cross-sections for each element and orbital provided by Yeh *et al.*,⁴¹ as well as with incident photon flux (provided in Fig. S1, ESI†). Elemental ratios were established by dividing the normalized signal intensity for two different elements at similar MEDs. Elemental ratios were computed for the four MEDs. The steps used to calculate elemental ratios are further explained in Brundle *et al.*³⁸

In partial Auger–Meitner electron yield NEXAFS measurements, Auger–Meitner electrons were detected instead of photoelectrons. These measurements were performed at the oxygen K-edge to investigate the chemical environment of



oxygen atoms in the samples. The resulting spectra provide additional and complementary information to XPS measurements, such as information regarding oxygen-containing species on the natural salt sample surfaces, interactions between these species and water vapor, and changes induced by exposure to ammonia. Partial Auger–Meitner electron yield NEXAFS measurements were conducted simultaneously with XPS to gain a comprehensive understanding of both surface composition and surrounding environment under varying exposure and partial pressures of water vapor and ammonia.

3. Results and discussion

3.1 Surface elemental composition

The surface elemental compositions of the MA Salt Lake brine and DLT Playa salt samples, upon exposure to different RH and partial pressures of NH_3 , were established with wide range photoemission (also named survey) spectra. These spectra, displayed in Fig. 1, reveal the presence of oxygen (O 1s), nitrogen (N 1s), carbon (C 1s), chlorine (Cl 2s and Cl 2p), sulfur (S 2p) and magnesium (Mg 2s and Mg 2p). However, the spectra do not show the presence of sodium (Na 2s), despite IC measurements indicating a high molar fraction of Na^+ (Table 1). This absence cannot be attributed to a low photoionization cross-section, as at a photon energy of 1000 eV, the photoionization cross-section of Na 2s is comparable to those of Mg 2s and Mg 2p. This suggests that Na^+ is depleted from the natural salt surface, a phenomenon we previously observed with APXPS measurements on natural salt samples collected in the Qaidam Basin.^{11,42} This phenomenon was also observed

with aerosol-in-flight XPS analysis of different salt particles.⁴³ The Na^+ depletion observed in our experiments is likely the result of sequential salt efflorescence, wherein, as RH decreases, NaCl crystallizes first on the sample holder surface, followed by crystallization of other salt species atop the NaCl layer. For example, efflorescence experiments on NaCl– MgCl_2 mixtures with varying mixing ratios have shown that upon decreasing RH, NaCl crystallizes first, followed by the co-crystallization of MgCl_2 and NaCl.⁴⁴

In the NH_3 -free cases (only water vapor), the survey spectra for the MA Salt Lake brine and DLT Playa salt samples at lowest RH levels (6 and 7%) in Fig. 1a and b appear to have no significant differences. Similarly, the survey spectra of MA Salt Lake brine and DLT Playa salt samples at higher RH levels (25%) in Fig. 1c and d exhibit no noticeable differences. Additionally, comparing survey spectra obtained at lowest RH (6 and 7%) and at highest RH (25%), shown in Fig. 1a and b with Fig. 1c and d, respectively, shows no significant differences, apart from the appearance of an additional peak for O 1s located at higher BE, which comes from the additional water vapor. That is, the presence of this peak is due to the increase in water vapor partial pressure in the near ambient pressure cell. Thus, the survey spectra acquired with addition of solely water vapor suggest that the surface composition of both natural salts remains relatively consistent, regardless of changes in RH and differences in the bulk ionic content.

In the NH_3 -exposed cases (water vapor and mix of NH_3/N_2), the peaks in the survey spectra of MA Salt Lake brine and DLT Playa salt in Fig. 1e and f exhibit an increase in intensity compared to those with water vapor only in Fig. 1a–d. This increase is particularly noticeable for the nitrogen (N 1s),

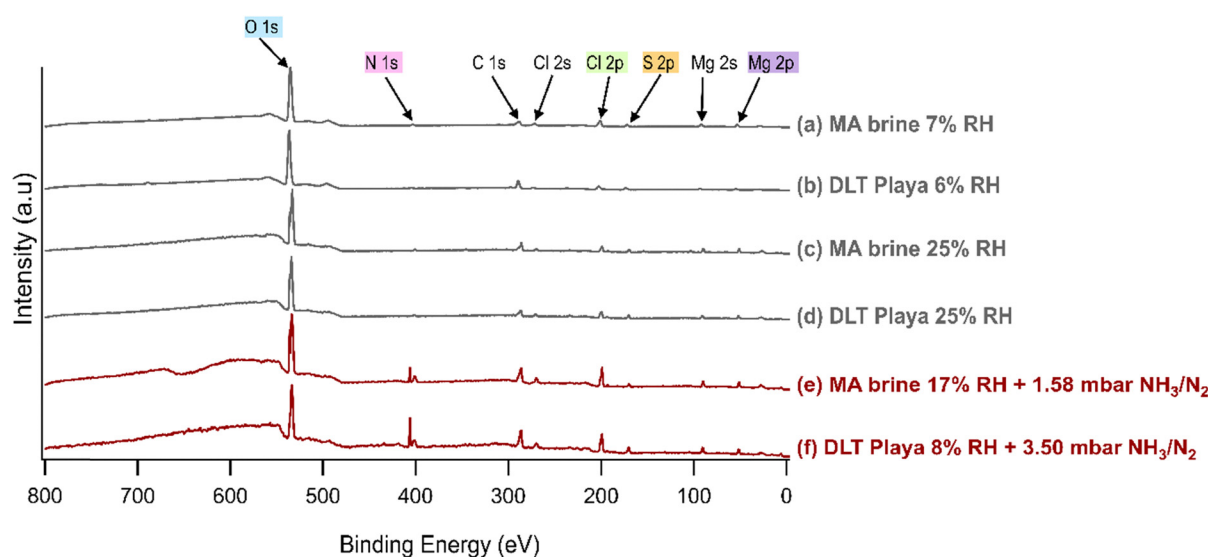


Fig. 1 Wide-range photoemission spectra of solid natural salts from MA Salt Lake brine and DLT Playa salt samples. Measurements were carried out at different RH and with the addition of NH_3/N_2 mixture (1% NH_3 in N_2). The intensity is given in arbitrary units (a.u.). In grey (a)–(d) are the spectra acquired with varying RH only while in dark red (e) and (f) are the spectra acquired with varying RH and the addition of a mix NH_3/N_2 . The photon energy used for these measurements is 1000 eV. The corresponding elements and orbitals for the major peaks are indicated above the arrows, with those highlighted representing those for which high-energy resolution photoemission spectra were also acquired. All spectra were normalized to the O 1s peak from (a) MA Salt Lake brine 7% RH.



carbon (C 1s), and chlorine (Cl 2s and Cl 2p) peaks. This increase cannot be attributed to gas-phase attenuation, which would reduce the signal of all elements equally. Instead, the relative reduction of the oxygen peak intensity suggests that NH_3 exposure causes a change in the surface composition, favoring species with lower oxygen content. Such a modification in the surface composition may arise from NH_4^+ formation on surfaces, as it is detected by the high-energy resolution photoemission spectra in Fig. 2.

3.2 Surface chemical composition

In XPS, elements in different oxidation states or different bonding environments can cause shifts in electron BE, often referred to as chemical shifts. High-energy resolution XPS spectra allow for the detection of these shifts, which help to identify the chemical species associated with the measured elements. In this

study, high-energy resolution XPS spectra, shown in Fig. 2, were acquired for the MA Salt Lake brine and DLT Playa salt samples for NH_3 -free and NH_3 -exposed cases. These spectra were obtained for elements and orbitals O 1s, N 1s, S 2p, Mg 2p and Cl 2p.

In the O 1s spectra, surface water ($\text{H}_2\text{O}_{(\text{sur})}$) and sulfate (SO_4^{2-}) peaks were detected for all conditions as shown in Fig. 2a, f, k and p. The separation in O 1s electron BE between $\text{H}_2\text{O}_{(\text{sur})}$ and SO_4^{2-} is approximately 1.20 eV, which is consistent with previous studies.^{11,12} An additional peak for water vapor ($\text{H}_2\text{O}_{(\text{gas})}$) is also observed in Fig. 2f, k and p. The absence of a signal for water vapor in Fig. 2a is due to the low RH combined with the short distance between the sample surface and the aperture of the electron analyser.

In the N 1s spectra, peaks of ammonium (NH_4^+), nitrogen-containing organic compounds (C–N) likely to be primary

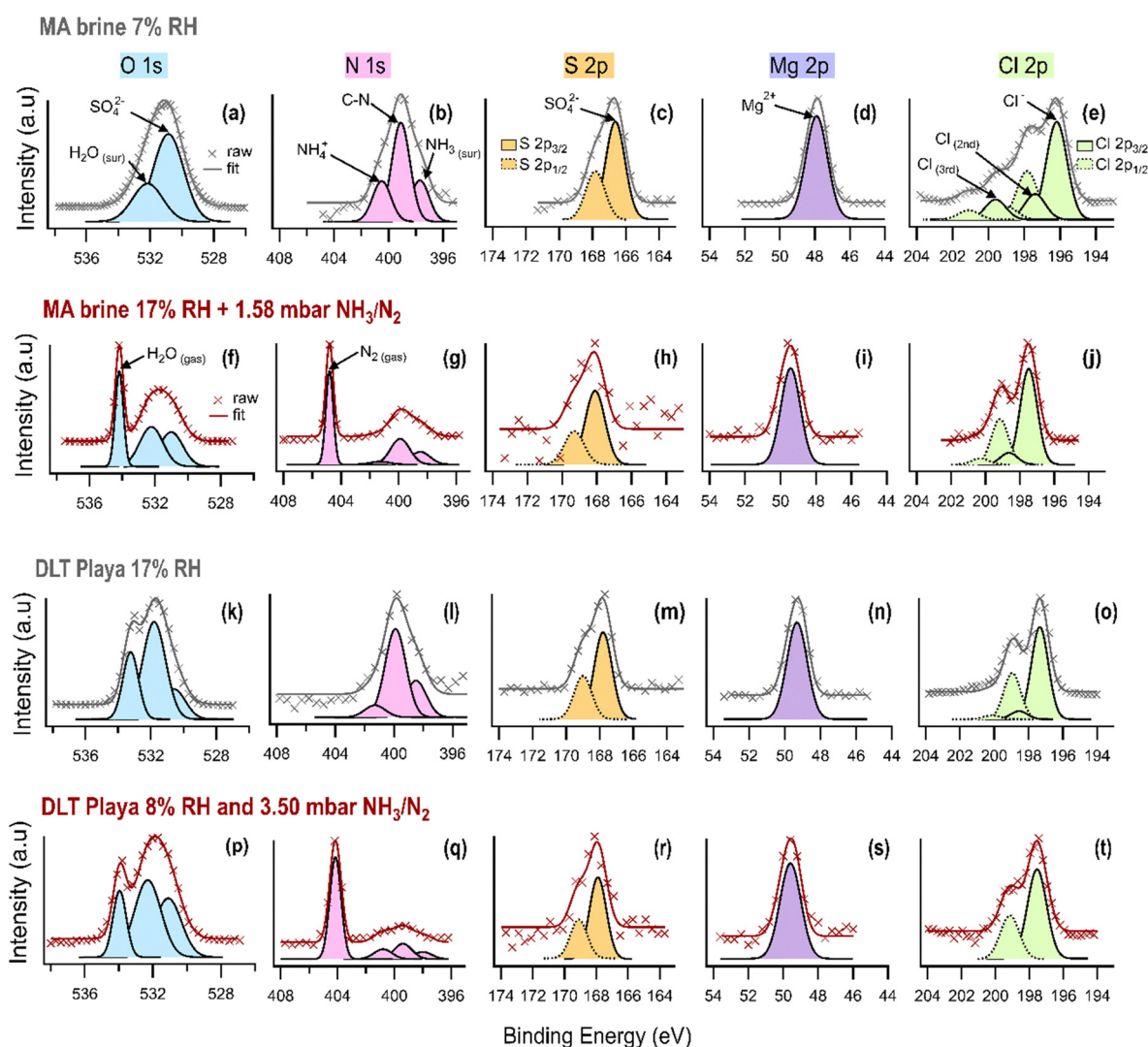


Fig. 2 High resolution XPS spectra of solid natural salts from MA Salt Lake brine and DLT Playa salt samples, for elements and orbitals O 1s, N 1s, S 2p, Mg 2p and Cl 2p. The intensity is given in arbitrary units (a.u.). Measurements were carried out at different RH and with the addition of NH_3/N_2 mixture (1% NH_3 in N_2). In grey ((a)–(e) and (k)–(o)) are the spectra acquired with varying RH only, while in dark red ((f)–(j) and (p)–(t)) are the spectra acquired with varying RH and the addition of NH_3/N_2 mixture. The binding energies are aligned to aliphatic C 1s at 284.8 eV. The spectra were acquired with different photon energies to fix the kinetic energy consistently at 300 eV.



amines (R-NH_2), and surface ammonia ($\text{NH}_{3(\text{sur})}$) were detected for all conditions as shown in Fig. 2b, g, l and q. An extra peak for nitrogen gas ($\text{N}_{2(\text{gas})}$) was observed in the N 1s spectra in Fig. 2g and q. The separation in N 1s electron BE between NH_4^+ and C–N is approximately 1.20 eV while the separation between NH_4^+ and $\text{NH}_{3(\text{sur})}$ is approximately 2.70 eV, which agrees with the values obtained by core electron binding energy (CEBE) calculations in previous studies.^{15,45} The presence of primary amines on sample surfaces is likely due to the NH_3 reaction with organic species from carbon contamination.⁴⁶ Additionally, high-energy resolution XPS spectra of C 1s in Fig. S7 and S13 (ESI†) show an increase in peaks related to oxidized carbon (C–O, C–N and C=O) in NH_3 -exposed cases, likely indicating an increasing amount of nitrogen containing organic compounds.

For S 2p spectra shown in Fig. 2c, h, m and r, deconvolution was carried out with spin–orbit coupling separation (between S 2p_{3/2} and S 2p_{1/2}) of 1.60 eV resulting in one single species, sulfate. Similarly, Mg 2p spectra shown in Fig. 2d, i, n and s were deconvoluted with one single species, the magnesium cation. For the Cl 2p spectra shown in Fig. 2e, j, o and t, deconvolution was carried out with a spin–orbit coupling separation of 1.20 eV resulting in different numbers of species for different natural salt samples and conditions. Most of the species were obtained for the Cl 2p spectra of the MA Salt Lake brine sample at 7% RH, as

shown in Fig. 2e, for which deconvolution is best represented with three species. At the lowest BE, the peak observed is associated with chloride species, while the assignment of the peaks to chlorine-containing species at higher BE, labeled chlorine second species ($\text{Cl}_{(2\text{nd})}$) and chlorine third species ($\text{Cl}_{(3\text{rd})}$), is more delicate. The separation in Cl 2p_{3/2} electron BE between Cl^- and $\text{Cl}_{(2\text{nd})}$ is approximately 1.20 eV, which is similar to the value obtained with CEBE calculations for HCl species on a NaCl salt surface, thus $\text{Cl}_{(2\text{nd})}$ may correspond to HCl.¹⁷ The separation between Cl^- and $\text{Cl}_{(3\text{rd})}$ is approximately 3.20 eV, which is too little to be chlorine oxides and instead may be organochlorine. Previous XPS measurements have revealed a separation of 3.30 eV between the chloride anion and organochlorine.⁴⁷

3.3 Elemental ratios

3.3.1 Comparison of elemental ratios at similar MED.

Elemental ratios in Fig. 3 provide insights into the relative concentration of elements at each of the four MED (1.1, 1.4, 1.5 and 1.7 nm below the surface). These ratios are calculated by dividing the normalized signal intensity of two different elements at a similar MED (from high-energy resolution XPS spectra in Fig. 2). In the NH_3 -free cases (grey lines), MA Salt Lake brine and DLT Playa salt samples exhibit similar elemental ratios at similar MED, suggesting similar surface elemental

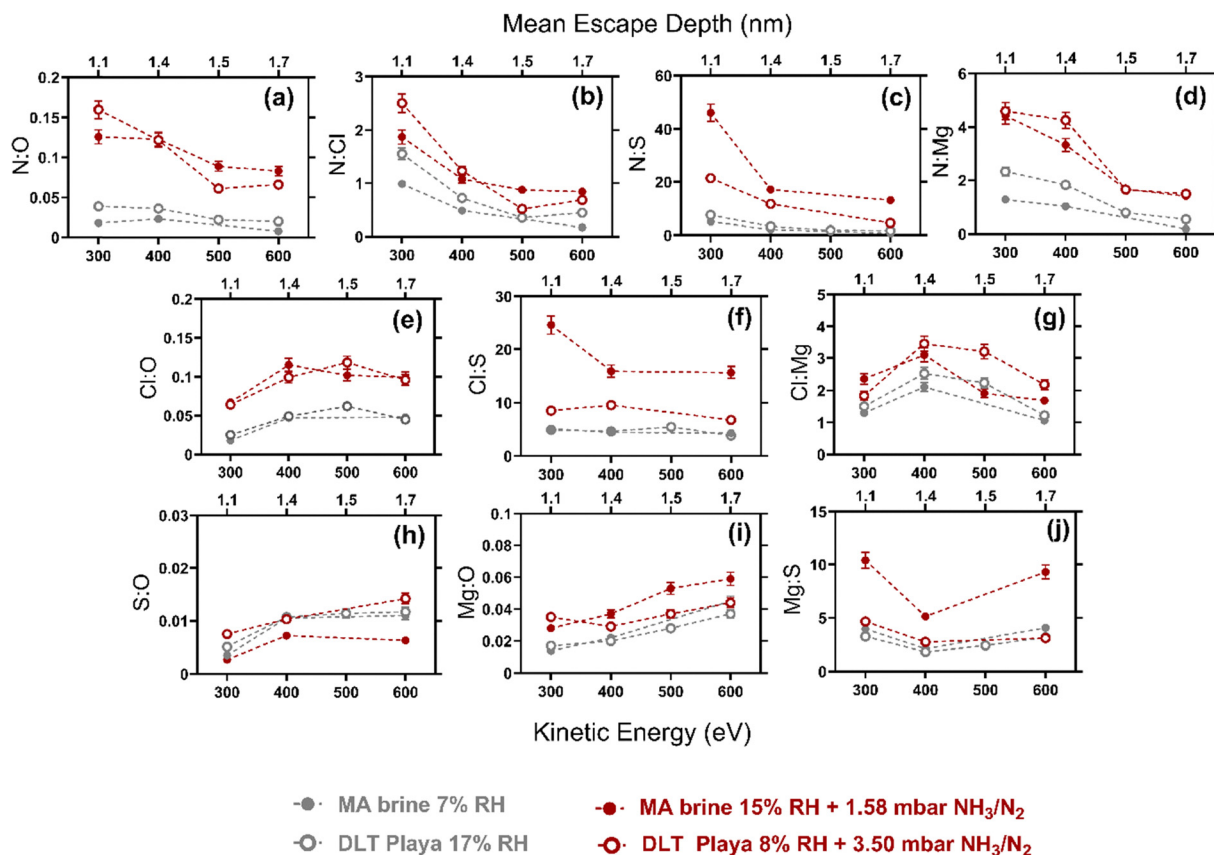


Fig. 3 Elemental ratios with increasing MED for solid natural salts from MA Salt Lake brine and DLT Playa salt samples. Elemental ratios include (a) N : O, (b) N : Cl, (c) N : S, (d) N : Mg, (e) Cl : O, (f) Cl : S, (g) Cl : Mg, (h) S : O, (i) Mg : O and (j) Mg : S. For elemental ratios including N and O elements, the contributions of the gas-phase signal, respectively, nitrogen and water vapor, were removed to only account for surface species.



compositions despite differences in their ionic bulk compositions, which is in agreement with previous observations made from survey spectra in Fig. 1. The similarity in the surface composition is likely due to the low MED, which corresponds to only a few molecular layers and may not reflect bulk differences. In the NH_3 -exposed cases (red lines), the elemental ratios at similar MED for both samples differ from their respective NH_3 -free cases.

The nitrogen-to-element ratios for both samples (with N_2 gas-phase signal excluded), including N:O, N:Cl, N:S and N:Mg in Fig. 3a–d, are higher in the NH_3 -exposed cases compared to NH_3 -free cases. These increases with the addition of NH_3 confirm the uptake of nitrogen-containing species on the sample surfaces, appearing as surface-adsorbed NH_3 , NH_4^+ and nitrogen-containing organic compounds, as shown in the N 1s high-energy resolution XPS spectra in Fig. 2g and q. The exclusion of contributions from the N_2 gas ensures that these increases are solely attributed to surface species.

The chlorine-to-element ratios for both samples, including Cl:O, Cl:S, and Cl:Mg in Fig. 3e–g, are higher in the NH_3 -exposed cases compared to NH_3 -free cases. This indicates that the presence of NH_4^+ drives Cl^- ions towards the surface, resulting in an enrichment of Cl^- where NH_4^+ is concentrated. The surface enrichment of Cl^- suggests the possibility of a subsequent release of gas-phase chlorinated species, as migration of Cl^- ions to the outermost layers increases their susceptibility to volatilization.²⁸ Furthermore, Cl:Mg elemental ratios exhibit values close to that of pure MgCl_2 (Cl:Mg = 2), indicating the likely presence of MgCl_2 -rich phases on the salt surfaces.

The element-to-sulfur ratios for both samples, including N:S, Cl:S and Mg:S ratios in Fig. 3c, f and j are higher in the NH_3 -exposed cases compared to NH_3 -free cases. These increases indicate that Cl^- appears to outcompete SO_4^{2-} for cation–anion neutralization of NH_4^+ ions. This phenomenon can result from preferential affinity between NH_4^+ and Cl^- compared to SO_4^{2-} , or it can be a consequence of the higher ionic molar fraction of Cl^- over SO_4^{2-} in the bulk (Table 1), which increases the likelihood of NH_4^+ pairing with Cl^- instead of SO_4^{2-} . This dynamics also implies that hydroxide ions (OH^-), produced from water deprotonation during NH_4^+ formation, are outcompeted by Cl^- . These reactive OH^- ions may be lost through oxidation of organic compounds, as suggested by the high-energy resolution XPS spectra for C 1s in Fig. S7 and S13 (ESI[†]) that reveal an increase in oxidized carbon in the NH_3 -exposed cases compared to NH_3 -free cases. Additionally, the increase in Cl:S ratios from NH_3 -free cases compared to NH_3 -exposed cases does not correlate with variations in RH. Specifically, the RH for the MA Salt Lake brine increases from 7% to 15%, while for the DLT Playa salt it decreases from 17% to 8%. This suggests that the observed increase in chloride ions relative to sulfate on the sample surfaces cannot be attributed solely to changes in RH.

Additionally, the increase of element-to-sulfur ratios upon NH_3 exposure is more significant in the MA Salt Lake brine sample compared to the DLT Playa salt sample. Correspondingly, the S:O ratio in Fig. 3h exhibits a decrease upon NH_3 exposure for

the MA Salt Lake brine sample while no significant change is observed for the DLT Playa salt sample. This indicates that SO_4^{2-} is further suppressed on the surface of the MA Salt Lake brine. When comparing the bulk compositions of the MA Salt Lake brine and DLT Playa salt samples, the primary difference is that the MA Salt Lake brine has a considerably higher Mg^{2+} fraction and a lower Na^+ fraction than DLT Playa salt, despite similar surface compositions observed in the XPS survey. Notably, no Na^+ ions were detected on the surfaces of either MA Salt Lake brine or DLT Playa salt samples, suggesting that Mg^{2+} is more surface-enriched compared to Na^+ in these salt mixtures. This surface enrichment of Mg^{2+} over Na^+ may play a role in the differential SO_4^{2-} depletion observed between the two samples. Further theoretical modelling may be required to rationalize the intricate ion pairing dynamics among different di/monovalent ions on the surface of weakly hydrated crystals at different RH and ionic compositions.

3.3.2 Comparison of elemental ratios with increasing MED. Elemental ratio variations with increasing MED (from 1.1 to 1.7 nm below the surface) provide insights into the distribution of elements along the probed MED. These variations are compiled as trends in Table 2. A consistent increase in elemental ratios with increasing MED is classified as an increasing trend (\uparrow), while a consistent decrease is classified as a decreasing trend (\downarrow). If no significant changes or alternating increases and decreases are observed in the elemental ratios with increasing MED, it is classified as no trend ($-$).

A decreasing trend with increasing MED is observed for all nitrogen-to-element ratios of both samples, including N:O, N:S, N:Mg and N:Cl in Fig. 3a–d. This suggests that nitrogen-containing species are enriched at the topmost molecular layers of the sample surfaces, even before NH_3 dosing. These nitrogen-containing species present before NH_3 dosing are potentially coming from the sample itself or can be due to contamination from previous experiments involving NH_3 dosing, such as desorption from the chamber walls of the near ambient pressure cell. A decreasing trend with increasing MED is observed for all element-to-oxygen ratios of both samples, including Cl:O, S:O and Mg:O, in Fig. 3e, h and i. This trend is coherent with water uptake on the natural salt sample surfaces, which is greater for the topmost molecular layers.

Table 2 Trends in elemental ratios with increasing mean escape depth for MA Salt Lake brine and DLT Playa salt for NH_3 -free cases and NH_3 -exposed cases. The trends are classified as increasing (\uparrow), decreasing (\downarrow) and no trend ($-$)

Ratio	NH_3 -free cases		NH_3 -exposed cases	
	MA	DLT	MA	DLT
(a) N:O	\downarrow	\downarrow	\downarrow	\downarrow
(b) N:S	\downarrow	\downarrow	\downarrow	\downarrow
(c) N:Mg	\downarrow	\downarrow	\downarrow	\downarrow
(d) N:Cl	\downarrow	\downarrow	\downarrow	\downarrow
(e) Cl:O	\uparrow	\uparrow	\uparrow	\uparrow
(f) Cl:S	$-$	$-$	$-$	$-$
(g) Cl:Mg	$-$	$-$	$-$	$-$
(h) S:O	\uparrow	\uparrow	\uparrow	\uparrow
(i) Mg:O	\uparrow	\uparrow	\uparrow	\uparrow
(j) Mg:S	$-$	$-$	$-$	$-$



No trend with increasing MED is observed for Cl:S, Cl:Mg and Mg:S ratios in Fig. 3f, g and j, suggesting that these elements are uniformly distributed within the probed MED.

3.4 Partial Auger–Meitner electron yield NEXAFS

The addition of water vapor and ammonia to the MA Salt Lake brine and DLT Playa salt samples induces notable changes in the partial Auger–Meitner electron yield NEXAFS oxygen K-edge spectra, as illustrated in Fig. 4. The spectra are divided into four regions: (I) 530–531.5 eV and (II) 534–536 eV, (III) 536.5–538.5 eV, and (IV) 540–543.5 eV.

In region I (530–531.5 eV), the feature has been previously associated with the electronic transition from the 1a1 molecular orbital to the 2b1* unoccupied molecular orbital in nitrate ($\text{N}=\text{O}$),⁴⁸ as well as the electronic transition from the oxygen 1s orbital into the π^* unoccupied molecular orbitals in carbonyl or carboxyl functions ($\text{C}=\text{O}$).⁴⁹ Here, no nitrate species are observed in the high-energy resolution XPS spectra in Fig. 2b, g, l and q nor in the IC results in Table 1, hence the feature observed in region I

is not likely from nitrate. Rather, this feature most probably comes from carbonyl or carboxyl functions, most probably attributable to carbon contamination. The presence of oxidized carbon species on both MA Salt Lake brine and DLT Playa salt sample surfaces is notably revealed by high-energy resolution XPS spectra for C 1s in Fig. S7 and S13 (ESI[†]). Such contamination is a common problem in APXPS.⁵⁰ Here, carbon contamination is particularly prominent at low RH (6 and 7%), with the highest intensity observed at 7% RH for the MA Salt Lake brine sample, in Fig. 4a and b, and 6% RH for the DLT Playa salt sample, in Fig. 4c and d. In the NH_3 -exposed cases, the intensity of this feature diminishes significantly, likely due to NH_4^+ formation on the surface. Nonetheless, previous studies reported features at photon energies similar to region I to be associated with other species, including metal oxides, such as magnesium oxide (MgO), and species containing oxygen–oxygen (O–O) bonds, such as peroxide ions.^{51,52} Notably, peroxide ions have been identified as responsible for the feature at 530.3 eV in amorphous alumina (Al_2O_3), with their formation believed to be induced by X-ray photon

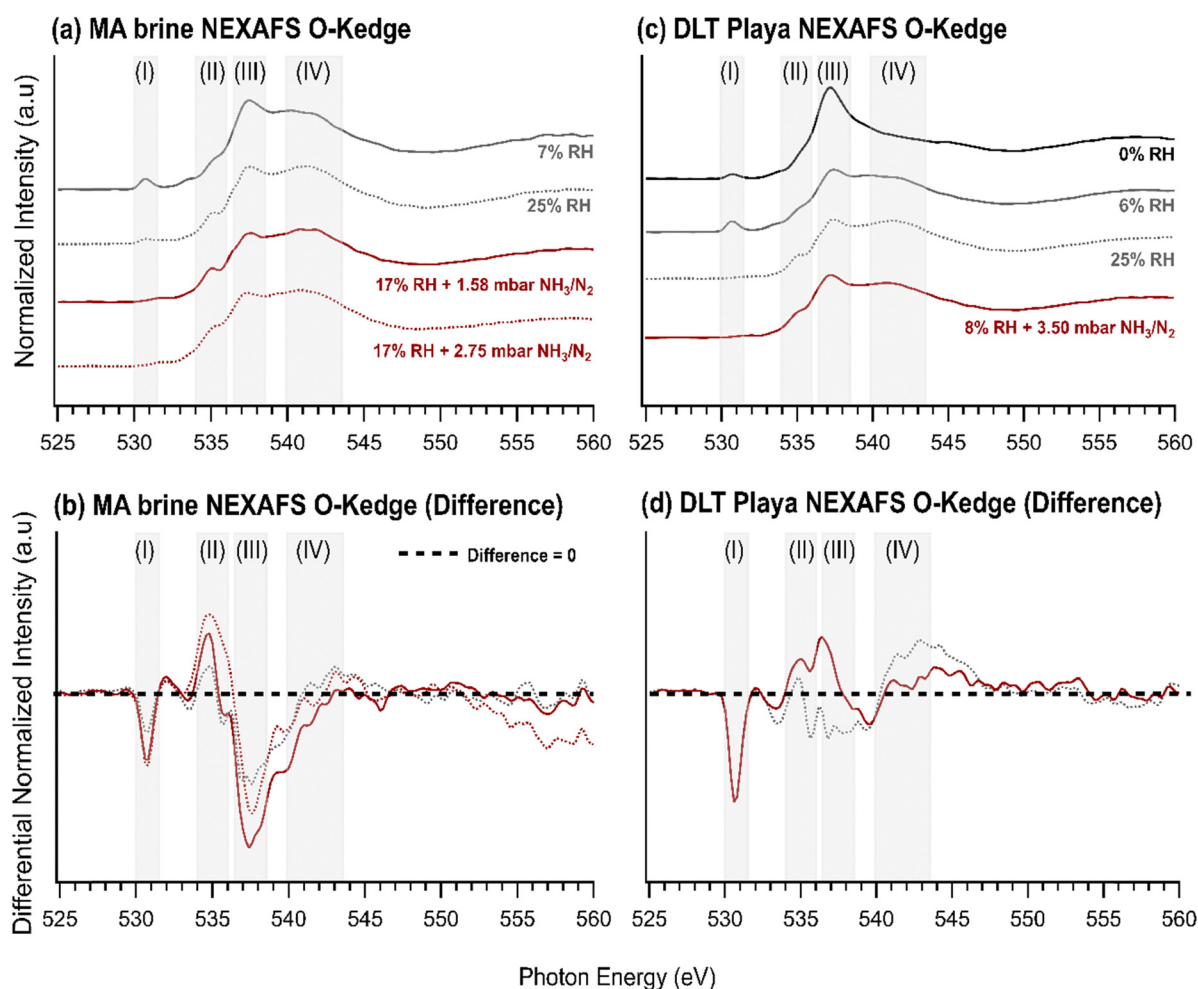


Fig. 4 Partial Auger–Meitner electron yield NEXAFS spectra of oxygen K-edge for solid natural salts from brine (a) and (b) and salt (c) and (d) samples of MA Salt Lake and DLT Playa, respectively. These spectra were taken at different RH and partial pressures of the NH_3/N_2 mixture. Edge-jump normalization of the spectra of MA Salt Lake brine (a) and (b) and DLT Playa salt (c) and (d) was performed using the energy regions 525–530 eV and 547–552 eV. Differential spectra for MA Salt Lake brine (b) were obtained by subtracting the oxygen K-edge spectra at 7% RH after normalization. Similarly, differential spectra for DLT Playa salt (d) were obtained by subtracting the oxygen K-edge spectra at 6% RH after normalization.



irradiation.⁵³ Regarding the complex chemical composition of the samples, the experimental conditions, and the likely amorphous nature of the salt surfaces, the presence of these species on the salt surfaces cannot be excluded.

Region II (534–536 eV) has been previously associated with uncoordinated water molecules in liquid water and on ice surfaces.^{51,54} Here, the intensity of region II in the difference spectra of MA Salt Lake brine and DLT Playa salt (Fig. 4b and d) increases with increasing RH. More water is taken up and observed at higher RH, thus increasing the intensity with increasing RH because more uncoordinated water molecules are present on the surface. The intensity in region II increases even further in the NH₃-exposed cases, likely due to NH₄⁺ formation on the surface, which consequently increases the amount of uncoordinated water molecules. Additionally, an energy shift towards higher energy can be observed in the difference spectra, notably for MA Salt Lake brine exposed to 17% RH and 2.75 mbar of the NH₃/N₂ mixture in Fig. 4b. Energy shifts were previously reported upon addition of alkali metal ions in liquid water and subsequent hydration of ions, with cations having a more pronounced effect than anions.⁵⁵ Here, the shift towards higher energy could be related to NH₄⁺ formation on the salt surfaces and their subsequent hydration.

Region III (536.5–538.5 eV) is linked to oxygen atoms in sulfate, and similar features have been observed in (NH₄)₂SO₄ and MgSO₄.^{11,56} In the differential spectra for MA Salt Lake brine (Fig. 4b), region III exhibits negative values, which are even more negative in the NH₃-exposed cases. This suggests that upon the addition of water vapor and ammonia, the presence of sulfate on the sample surface diminishes, consistent with the elemental ratios shown in Fig. 3. Contrastingly, for the DLT Playa salt, changes in region III are less pronounced. This is also consistent with Fig. 3, where the element-to-sulfur ratios for DLT Playa salt (N:S, Cl:S, and Mg:S in Fig. 3c, f, and j) exhibit a smaller increase from NH₃-free cases to NH₃-exposed cases in comparison with MA Salt Lake brine. Nonetheless, the differential spectra of DLT Playa salt with subtraction of NEXAFS O-Kedge spectra at 0% RH (Fig. S14, ESI†) exhibit negative values, suggesting that exposure to a humidified atmosphere decreases sulfate ions on the salt surface. This may result from competition between chloride and sulfate for solvation, as suggested by molecular dynamics simulations in our previous study, which showed that on a MgCl₂·8H₂O crystal, Cl[−] exhibits a greater tendency for solvation than SO₄^{2−}.¹¹

Region IV (540–543.5 eV) corresponds to adsorbed water, as indicated by previous studies showing its growth with increasing RH.^{11,12,57} Here, region IV increases in intensity as RH rises for both MA Salt Lake brine and DLT Playa salt samples. This behavior is consistent with the expected uptake of water at natural salt samples surfaces, particularly at higher RH levels.

4. Atmospheric implications

The phenomena observed in this study may have important implications for atmospheric processes involving primary

natural salt particles, such as atmospheric chemistry and cloud properties. The enrichment of Cl[−] on the salt sample surfaces suggests an increase likelihood for its volatilization. This volatilization, known as the dechlorination process, has been widely studied for pure salt systems, both solid and deliquesced. In these systems, acid displacement reactions driven by the addition of acidic compounds (*e.g.*, HNO₃, H₂SO₄) or the oxidation reaction by atmospheric oxidants (*e.g.*, N₂O₅, NO_x, O₃) are considered as the main pathways.^{28,29,58} However, studies involving more complex salt systems such as natural salts are limited, particularly for low RH conditions.^{27,28} Here, we show that the dechlorination process could also occur in complex salt systems, highlighting its potential occurrence in the atmosphere on primary natural salt particle surfaces from terrestrial sources. The release of chlorine-containing gas-phase compounds has important consequences for atmospheric chemistry, as they affect stratospheric ozone and air pollution.^{16,27,30,59}

The increased amount of NH₄⁺ on the salt surfaces reveals the conversion of NH₃ to NH₄⁺ under low RH conditions. In the atmosphere, the gas-to-particle conversion of NH₃, a highly soluble base, to NH₄⁺ is primarily known to occur in aqueous phase reactions, but some studies have shown that this process can also occur on solid aerosol particles, such as sulfuric acid and organic acid particles.^{60–62} Here we show that gas-to-particle conversion of NH₃ to NH₄⁺ could also occur on the surfaces of solid primary natural salt particles, thereby leading to the formation of SIAs. This finding enhances our understanding of gas-to-particle conversion processes, particularly in regions where primary natural salt particles are abundant and dry conditions (low RH levels) prevail.

The simultaneous increase in Cl[−] and NH₄⁺ on the surface of solid natural salt samples suggests the potential formation of NH₄Cl, or, upon dechlorination, the possible formation of other ammonium salts such as (NH₄)₂SO₄. In the atmosphere, the chemical composition of primary natural salt particles plays a crucial role in determining their impact on cloud properties, particularly regarding droplet and ice crystal formation. For droplet formation, the cloud condensation nuclei (CCN) activity of salts varies significantly with their composition.⁶³ For ice formation, (NH₄)₂SO₄ has been identified as an important ice nucleating particle (INP) by deposition freezing mode in the atmosphere, notably for cirrus clouds.⁶⁴ Additionally, the NH₄⁺ ion has been shown to promote the ice nucleation activity of mineral feldspar through immersion freezing.⁶⁵ This effect is particularly relevant for primary natural salt particles in arid regions, as they are often mixed with mineral dust particles.^{4,5,66–68}

5. Conclusions

This study investigates phenomena occurring on surfaces of solid natural salt samples upon addition of NH₃ under low RH conditions. In NH₃-free cases (water vapor only), XPS results show evidence of water uptake on the sample surfaces. These results are supported by the presence of a feature for adsorbed water in the oxygen K-edge partial Auger–Meitner electron yield



NEXAFS spectra. In NH_3 -exposed cases (water vapor plus a mix of NH_3/N_2), XPS results reveal the uptake of nitrogen-containing species, along with surface enrichment of Cl^- ions. The Cl^- enrichment is likely driven by the formation of NH_4^+ on surfaces, for which cation-anion neutralization appears to be outcompeted by Cl^- rather than other anions such as SO_4^{2-} . This suggests a competitive dynamics between anions in the neutralization process. This description is supported by the oxygen K-edge partial Auger–Meitner electron yield NEXAFS spectra, wherein a decrease in the SO_4^{2-} feature and an increase in the feature associated with uncoordinated water likely from NH_4^+ formation are observed. The findings of this study highlight the need for deeper investigations into the mechanisms of ion interactions on surfaces of salts and their broader implications in atmospheric processes. Notably, the potential dechlorination process and modification in the physicochemical properties of the solid primary natural salt surfaces reveal potential impacts on air pollution, the stratospheric ozone layer and the water cycle.

Conflicts of interest

The authors declare no conflicts of interest.

Data availability

Data for this article, including APXPS and NEXAFS data are available at Zenodo at <https://doi.org/10.5281/zenodo.15031781>.

Acknowledgements

This project is supported by the Swedish Research Council VR (2021-04042) and Carl Tryggers Stiftelse Scientific Research Grant (CTS 23:2526). X. K. and E. S. T. acknowledge the support from the Swedish Foundation for International Cooperation in Research and Higher Education (CH2019-8361). E. S. T. and N. F. have been supported by the Swedish Research Councils VR (2020-03497). We acknowledge the MAX IV Laboratory for beamtime on the HIPPIE beamline under proposal 20220123. Research conducted at MAX IV, a Swedish national user facility, is supported by Vetenskapsrådet (Swedish Research Council, VR) under contract 2018-07152, Vinnova (Swedish Governmental Agency for Innovation Systems) under contract 2018-04969 and Formas under contract 2019-02496.

References

- X. Gong, J. Zhang, B. Croft, X. Yang, M. M. Frey, N. Bergner, R. Y. Chang, J. M. Creamean, C. Kuang, R. V. Martin, A. Ranjithkumar, A. J. Sedlacek, J. Uin, S. Willmes, M. A. Zawadowicz, J. R. Pierce, M. D. Shupe, J. Schmale and J. Wang, *Nat. Geosci.*, 2023, **16**, 768–774.
- A. Jilili and G. Mu, *Eurasian Soil Sci.*, 2006, **39**, 367–376.
- H. Zhu, W. Li, X. Kong and X. Zhang, *J. Geophys. Res.: Atmos.*, 2025, **130**, e2024JD042693.
- X. Wang, T. Hua, C. Zhang, L. Lang and H. Wang, *Atmos. Res.*, 2012, **118**, 1–9.
- X. Wang, T. Hua, C. Zhang, G. Qian and W. Luo, *Environ. Earth Sci.*, 2013, **68**, 623–631.
- M. Patanen, I. Unger, C.-M. Saak, G. Gopakumar, R. Lexelius, O. Björneholm, M. Salter and P. Zieger, *Environ. Sci.: Atmos.*, 2022, **2**, 1032–1040.
- X. Kong, C. Wu, H. R. Mishra, Y. Hao, M. Cazaunau, A. Bergé, E. Pangui, R. Faust, W. Liu, J. Li, S. Wang, B. Picquet-Varrault and M. Hallquist, *Atmos. Environ.*, 2024, **322**, 120373.
- J. Fan, L. Shao, Y. Hu, J. Wang, J. Wang and J. Ma, *Atmos. Pollut. Res.*, 2016, **7**, 833–842.
- M. E. Wise, S. T. Martin, L. M. Russell and P. R. Buseck, *Aerosol Sci. Technol.*, 2008, **42**, 281–294.
- D. Castarède and E. S. Thomson, *Atmos. Chem. Phys.*, 2018, **18**, 14939–14948.
- N. Fauré, J. Chen, L. Artiglia, M. Ammann, T. Bartels-Rausch, J. Li, W. Liu, S. Wang, Z. A. Kanji, J. B. C. Pettersson, I. Gladich, E. S. Thomson and X. Kong, *ACS Earth Space Chem.*, 2023, **7**, 350–359.
- N. Fauré, J. Chen, L. Artiglia, M. Ammann, T. Bartels-Rausch, Z. A. Kanji, S. Wang, J. B. C. Pettersson, E. S. Thomson, I. Gladich and X. Kong, *ACS ES&T Air*, 2024, **1**, 1373–1382.
- K. Arima, P. Jiang, X. Deng, H. Bluhm and M. Salmeron, *J. Phys. Chem. C*, 2010, **114**, 14900–14906.
- Z. Liu, A. Sinopoli, J. S. Francisco and I. Gladich, *J. Am. Chem. Soc.*, 2024, **146**, 17898–17907.
- X. Kong, D. Castarède, E. S. Thomson, A. Boucly, L. Artiglia, M. Ammann, I. Gladich and J. B. C. Pettersson, *Science*, 2021, **374**, 747–752.
- R. Karlsson and E. Ljungström, *J. Aerosol Sci.*, 1995, **26**, 39–50.
- X. Kong, I. Gladich, N. Fauré, E. S. Thomson, J. Chen, L. Artiglia, M. Ammann, T. Bartels-Rausch, Z. A. Kanji and J. B. C. Pettersson, *J. Phys. Chem. Lett.*, 2023, **14**, 6151–6156.
- H. C. Allen, J. M. Laux, R. Vogt, B. J. Finlayson-Pitts and J. C. Hemminger, *J. Phys. Chem.*, 1996, **100**, 6371–6375.
- H. Xiong, J. K. Lee, R. N. Zare and W. Min, *J. Phys. Chem. Lett.*, 2020, **11**, 7423–7428.
- H. Hao, I. Leven and T. Head-Gordon, *Nat. Commun.*, 2022, **13**, 280.
- M. Crippa, D. Guizzardi, M. Muntean, E. Schaaf, F. Dentener, J. A. van Aardenne, S. Monni, U. Doering, J. G. J. Olivier, V. Pagliari and G. Janssens-Maenhout, *Earth Syst. Sci. Data*, 2018, **10**, 1987–2013.
- J. H. Seinfeld and S. N. Pandis, *Atmospheric chemistry and physics: from air pollution to climate change*, John Wiley & Sons, Inc., Hoboken, New Jersey, 2016.
- C. Wu, S. Zhang, G. Wang, S. Lv, D. Li, L. Liu, J. Li, S. Liu, W. Du, J. Meng, L. Qiao, M. Zhou, C. Huang and H. Wang, *Environ. Sci. Technol.*, 2020, **54**, 15622–15630.
- Q. Shi, P. Davidovits, J. T. Jayne, D. R. Worsnop and C. E. Kolb, *J. Phys. Chem. A*, 1999, **103**, 8812–8823.
- S. Chen, L. Artiglia, F. Orlando, J. Edebeli, X. Kong, H. Yang, A. Boucly, P. Corral Arroyo, N. Prisle and M. Ammann, *ACS Earth Space Chem.*, 2021, **5**, 3008–3021.



- 26 J. L. Thomas, A. Jimenez-Aranda, B. J. Finlayson-Pitts and D. Dabdub, *J. Phys. Chem. A*, 2006, **110**, 1859–1867.
- 27 D. Mitroo, T. E. Gill, S. Haas, K. A. Pratt and C. J. Gaston, *Environ. Sci. Technol.*, 2019, **53**, 7442–7452.
- 28 B. Su, T. Wang, G. Zhang, Y. Liang, C. Lv, Y. Hu, L. Li, Z. Zhou, X. Wang and X. Bi, *Atmos. Environ.*, 2022, **290**, 119365.
- 29 B. J. Finlayson-Pitts, *Chem. Rev.*, 2003, **103**, 4801–4822.
- 30 M. J. Molina, T. L. Tso, L. T. Molina and F. C. Wang, *Science*, 1987, **238**, 1253–1257.
- 31 R. A. VanCuren and T. A. Cahill, *J. Geophys. Res.: Atmos.*, 2002, **107**, 4804.
- 32 J. Xu, M. H. Bergin, R. Greenwald, J. J. Schauer, M. M. Shafer, J. L. Jaffrezo and G. Aymoz, *J. Geophys. Res.: Atmos.*, 2004, **109**, D19S03.
- 33 R. Arimoto, X. Y. Zhang, B. J. Huebert, C. H. Kang, D. L. Savoie, J. M. Prospero, S. K. Sage, C. A. Schloesslin, H. M. Khaing and S. N. Oh, *J. Geophys. Res.: Atmos.*, 2004, **109**, D19S04.
- 34 Y. Hao, Y. Qiu, J. Li, W. Liu, L. Chen, X. Zhang, M. Tang, Z. Niu, S. Wang and X. Kong, *ACS Earth Space Chem.*, 2024, **8**, 1111–1121.
- 35 A. Wang, P. Sobron, F. Kong, M. Zheng and Y.-Y. S. Zhao, *Astrobiology*, 2018, **18**, 1254–1276.
- 36 F. Kong, M. Zheng, B. Hu, A. Wang, N. Ma and P. Sobron, *Astrobiology*, 2018, **18**, 1243–1253.
- 37 S. Zhu, M. Scardamaglia, J. Kundsén, R. Sankari, H. Tarawneh, R. Temperton, L. Pickworth, F. Cavalca, C. Wang, H. Tissot, J. Weissenrieder, B. Hagman, J. Gustafson, S. Kaya, F. Lindgren, I. Kallquist, J. Maibach, M. Hahlin, V. Boix, T. Gallo, F. Rehman, G. D'Acunto, J. Schnadt and A. Shavorskiy, *J. Synchrotron Radiat.*, 2021, **28**, 624–636.
- 38 C. R. Brundle and B. V. Crist, *J. Vac. Sci. Technol., A*, 2020, **38**, 041001.
- 39 C. J. Powell, *J. Vac. Sci. Technol., A*, 2020, **38**, 023209.
- 40 S. Tanuma, C. J. Powell and D. R. Penn, *Surf. Interface Anal.*, 1994, **21**, 165–176.
- 41 J. J. Yeh and I. Lindau, *At. Data Nucl. Data Tables*, 1985, **32**, 1–155.
- 42 X. Kong, S. Zhu, A. Shavorskiy, J. Li, W. Liu, P. Corral Arroyo, R. Signorell, S. Wang and J. B. C. Pettersson, *Environ. Sci.: Atmos.*, 2022, **2**, 137–145.
- 43 E. Pelimanni, C.-M. Saak, G. Michailoudi, N. Prisle, M. Huttula and M. Patanen, *Phys. Chem. Chem. Phys.*, 2022, **24**, 2934–2943.
- 44 D. Gupta, H. J. Eom, H. R. Cho and C. U. Ro, *Atmos. Chem. Phys.*, 2015, **15**, 11273–11290.
- 45 J. Chen, G. W. Kisimbiri, I. Gladich, N. Fauré, E. S. Thomson, R. Temperton, Z. A. Kanji and X. Kong, *J. Phys. Chem. A*, 2025, **129**, 2922–2931.
- 46 K. M. Updyke, T. B. Nguyen and S. A. Nizkorodov, *Atmos. Environ.*, 2012, **63**, 22–31.
- 47 M. Wilson, R. Kore, A. W. Ritchie, R. C. Fraser, S. K. Beaumont, R. Srivastava and J. P. S. Badyal, *Colloids Surf., A*, 2018, **545**, 78–85.
- 48 A. Krepelova, J. Newberg, T. Huthwelker, H. Bluhm and M. Ammann, *Phys. Chem. Chem. Phys.*, 2010, **12**, 8870–8880.
- 49 H. Bluhm, D. F. Ogletree, S. F. Charles, H. Zahid and S. Miquel, *J. Phys.: Condens. Matter*, 2002, **14**, L227.
- 50 N. Comini, T. Huthwelker, J. T. Diulus, J. Osterwalder and Z. Novotny, *J. Vac. Sci. Technol., A*, 2021, **39**, 043203.
- 51 P. Wernet, D. Nordlund, U. Bergmann, M. Cavalleri, M. Odelius, H. Ogasawara, L. Å. Näslund, T. K. Hirsch, L. Ojamäe, P. Glatzel, L. G. M. Pettersson and A. Nilsson, *Science*, 2004, **304**, 995–999.
- 52 F. Frati, M. Hunault and F. M. F. de Groot, *Chem. Rev.*, 2020, **120**, 4056–4110.
- 53 T. Lindner, H. Sauer, W. Engel and K. Kambe, *Phys. Rev. B: Condens. Matter Mater. Phys.*, 1986, **33**, 22–24.
- 54 C. Århammar, A. Pietzsch, N. Bock, E. Holmström, C. M. Araujo, J. Gråsjö, S. Zhao, S. Green, T. Peery, F. Hennies, S. Amerioun, A. Föhlisch, J. Schlappa, T. Schmitt, V. N. Strocov, G. A. Niklasson, D. C. Wallace, J. Rubensson, B. Johansson and R. Ahuja, *Proc. Natl. Acad. Sci. U. S. A.*, 2011, **108**, 6355–6360.
- 55 M. Nagasaka, H. Yuzawa and N. Kosugi, *J. Phys. Chem. B*, 2017, **121**, 10957–10964.
- 56 V. Zelenay, M. Ammann, A. Křepelová, M. Birrer, G. Tzvetkov, M. G. C. Vernooij, J. Raabe and T. Huthwelker, *J. Aerosol Sci.*, 2011, **42**, 38–51.
- 57 X. Kong, D. Castarède, A. Boucly, L. Artiglia, M. Ammann, T. Bartels-Rausch, E. S. Thomson and J. B. C. Pettersson, *J. Phys. Chem. C*, 2020, **124**, 5263–5269.
- 58 M. J. Rossi, *Chem. Rev.*, 2003, **103**, 4823–4882.
- 59 X. Wang, D. J. Jacob, S. D. Eastham, M. P. Sulprizio, L. Zhu, Q. Chen, B. Alexander, T. Sherwen, M. J. Evans, B. H. Lee, J. D. Haskins, F. D. Lopez-Hilfiker, J. A. Thornton, G. L. Huey and H. Liao, *Atmos. Chem. Phys.*, 2019, **19**, 3981–4003.
- 60 J. J. Huntzicker, R. A. Cary and C.-S. Ling, *Environ. Sci. Technol.*, 1980, **14**, 819–824.
- 61 M. Sauerwein and C. K. Chan, *Atmos. Chem. Phys.*, 2017, **17**, 6323–6339.
- 62 M. C. Fairhurst, M. J. Ezell and B. J. Finlayson-Pitts, *Phys. Chem. Chem. Phys.*, 2017, **19**, 26296–26309.
- 63 M. D. Petters and S. M. Kreidenweis, *Atmos. Chem. Phys.*, 2007, **7**, 1961–1971.
- 64 J. P. D. Abbatt, S. Benz, D. J. Cziczo, Z. Kanji, U. Lohmann and O. Möhler, *Science*, 2006, **313**, 1770–1773.
- 65 T. F. Whale, *J. Chem. Phys.*, 2022, **156**, 144503.
- 66 M. D. Baer, I. F. W. Kuo, H. Bluhm and S. Ghosal, *J. Phys. Chem. B*, 2009, **113**, 15843–15850.
- 67 S. Ghosal, J. C. Hemminger, H. Bluhm, B. S. Mun, E. L. D. Hebenstreit, G. Ketteler, D. F. Ogletree, F. G. Requejo and M. Salmeron, *Science*, 2005, **307**, 563–566.
- 68 N. Ottosson, J. Heyda, E. Wernersson, W. Pokapanich, S. Svensson, B. Winter, G. Öhrwall, P. Jungwirth and O. Björneholm, *Phys. Chem. Chem. Phys.*, 2010, **12**, 10693–10700.

